RSC Advances

ROYAL SOCIETY OF CHEMISTRY

www.rsc.org/advances

Hierarchical mesoporous urchin-like and bundle-like Co_3O_4 were selectively synthesized via calcining the as-prepared novel precursor. The morphology evolution mechanism of the precursor was revealed through systematic time- and temperature-dependent experiments. The enhanced lithium storage properties of mesoporous urchin-like and bundle-like Co_3O_4 were investigated.

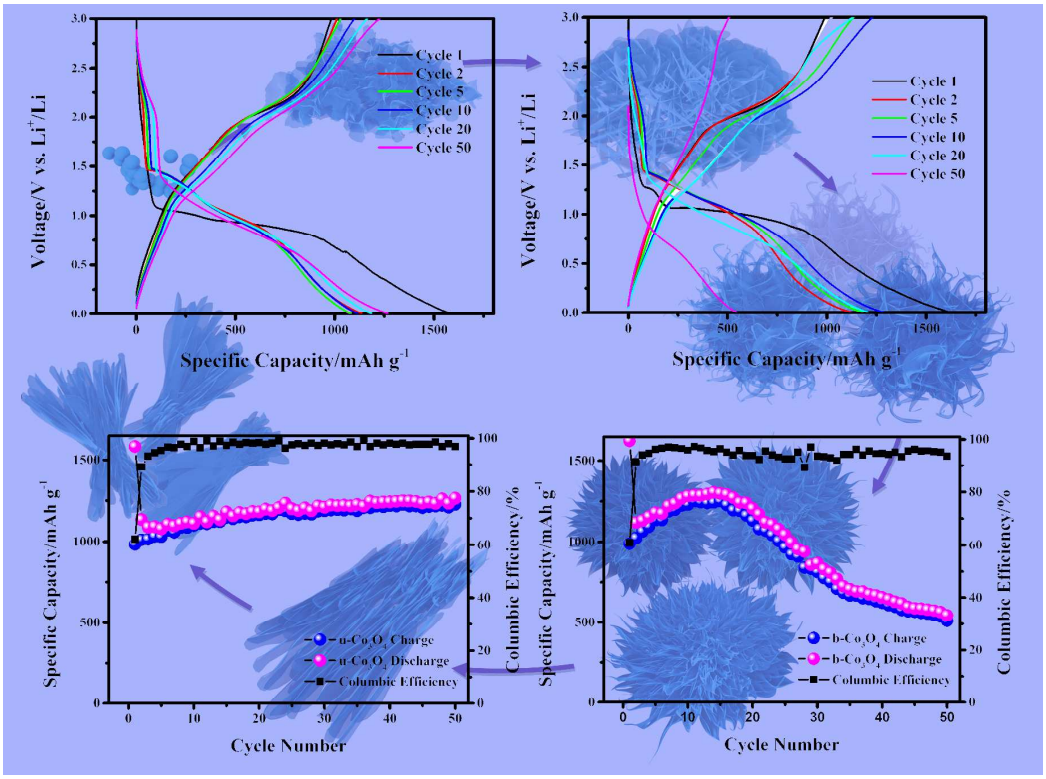

RSC Advances

RSCPublishing

ARTICLE

A facile strategy for fabricating hierarchically mesoporous Co_3O_4 urchins and bundles and their application in Li-ion batteries with high electrochemical performance

Cite this: DOI: 10.1039/x0xx00000x

Received 00th December 2014,
Accepted 00th January 2015

DOI: 10.1039/x0xx00000x

www.rsc.org/

Tao Yang, Yangai Liu*, Zhaohui Huang*, Qian Yang, Ming Guan, Minghao Fang, Xiaowen Wu

Herein, we report a facile template- and surfactant-free strategy for the fabrication of 3D hierarchically mesoporous Co_3O_4 urchins and bundles, which involves a subsequent heat treatment of the corresponding novel precursors at 400 °C in air for 4 h. The morphology evolution mechanism of the precursor was revealed through systematic time- and temperature-dependent experiments. The as-synthesized mesoporous Co_3O_4 urchins and bundles deliver an enhanced lithium storage capacity good cycling stability and excellent rate capabilities (e.g., 781 mAh g^{-1} for Co_3O_4 urchins and 660 mAh g^{-1} for Co_3O_4 bundles at 2 A g^{-1}), indicating their potential applications in high power lithium ion batteries. The improved electrochemical performance is mainly attributed to the 3D structure and numerous mesopores within the nanofiber and nanosheets, which can effectively enhance structural stability, provide the efficient diffusion length for lithium ions and electrons, and buffer volume expansion during the Li+ insertion/extraction processes.

Introduction

Lithium ion batteries (LIBs) have applied as the power source for portable electronic devices due to their high energy density, long life cycle and excellent safety over the past decades.[1-9] Considerable work have been devoted to the exploitation of novel anode materials with high rate properties, reversible capacity and long lifespan. Among various anode materials, transition metal oxide (e.g., Co_3O_4) has been considered as the dominant anodic candidate to replace commercial graphite since its high theoretical capacity (892 mA h g^{-1} for Co_3O_4). [10-14] However, the design of Co_3O_4 anodes with long-term stable lifespan is still of great challenge since it also suffer from low intrinsic electrical conductivity and large volume change during lithium insertion/extraction,[15] which results in its poor rate capability, cycling stability and hinders the practical utilization in advanced LIBs. Up to now, extensive efforts has proceeded to alleviate these above drawback via minimize the negative influence of particle agglomerations on the electrochemical properties and design microscopic structures. Among them, the design of the material with hierarchically porous micro-/nanostructures, which can provide more active reaction sites and shorten Li+ ions diffusion paths, has proven to be an effective strategy to improve their lithium-storage capabilities. It is general practice that the hierarchically porous Co_3O_4 micro-/nanostructures can be prepared through a two-step method using Co-based intermediate compounds, like cobalt-hydroxide-carbonate, cobalt carbonate ($CoCO_3$) or cobalt hydroxide ($Co(OH)_2$) as the precursor followed by thermal treatment in air. In this approach, the preparation of Co_3O_4 micro-/nanostructures with porous morphology is relatively less challenging.

In the present work, we report a facile template-free hydrothermal method to synthesize hierarchically urchin-like and bundle-like cobalt-hydroxide-carbonate micro-/nano-structures and their transformation to mesoporous Co_3O_4. Through the time-/temperature experiment, the morphology evolution mechanism of the precursor have been proposed, which can provide some ideas in the fabrication of hierarchically porous Co_3O_4 structures assembled by nano- wires or sheets to researchers. When measured as a potential anode for LIBs, the as-synthesized Co_3O_4 demonstrate improved lithium-storage capabilities in terms of reversible capacity, cycling stability, and rate capability. The excellent electrochemical performance can be attributed to their unique porous architecture.

Experimental

Synthesis

Synthesis of hierarchically mesoporous Co_3O_4 urchins and bundles. The cobalt-hydroxide-carbonate precursor was synthesized via a facile hydrothermal method. Briefly, 2 mmol of cobaltous sulfate and 30 mmol of urea were dissolved in 70 mL deionized

water to form a red solution. After stirring for 30 min, the mixture was tightly sealed in a Teflon-lined stainless steel autoclave and maintained at 90 °C for 36 h and 120 h, respectively. Then, the resulting products were washed with distilled water and ethanol and then dried at 60 °C in a vacuum oven. Finally, both the urchin-like and bundle-like precursor were kept in a tube furnace at 400 °C for 4 h in air at a ramping rate of 2 °C min^{-1}, resulting in mesoporous Co_3O_4 urchins and bundles, respectively. The Co_3O_4 urchins and bundles are marked as u-Co_3O_4 and b-Co_3O_4, respectively.

Materials Characterization

The morphology of the products were characterized by a MERLIN VP Compact scanning electron microscopy. Powder X-ray diffraction (XRD) measurements were performed by using Cu Kα radiation (λ = 0.15406nm). Thermogravimetric analysis (TGA) was examined on a thermal analyzer (TGA Q5000 IR) in air. X-ray photoelectron spectroscopy (XPS) analysis was collected on a Thermo Fisher ESCALAB 250 Xi spectrometer. The surface area of the as-annealed sample was investigated through measuring N2 adsorption–desorption isotherms at 77 K, using an Autosorb-iQ2-MP system. Fourier transform infrared (FT–IR) spectra were determined by a Bruker VERTEX70v FT-IR spectrophotometer, samples were prepared by using a standard KBr disk method.

Electrochemical Measurements

The electrodes were made as follows: 70 wt % the samples were mixed with 20 wt % Super P, and 10 wt % poly (vinylidene fluoride) in N-methyl-2-pyrrolidene to obtain the dark slurry. Then the slurry was coated on a piece of copper foils and dried at 120 °C for 24 h under vacuum. Electrochemical tests were examined by assembling a coin-type electrochemical cell (2032-type), which was prepared in an Ar-filled glovebox with lithium foil serving as the counter electrode and 1M $LiPF_6$ in a mixture of ethylene carbonate (EC)/dimethyl carbonate (DMC)/diethyl carbonate (DEC) (1:1:1, in wt%) as the electrolyte solution. A galvanostatic charging/discharging test of the as-assembled cell was examined on a battery tester (BT2043, Arbin Instrument) in the potential range of 0.005-3 V. All of the electrochemical measurements were conducted at 25 °C.

Results and discussion

The XRD patterns of the two kind of cobalt-hydroxide-carbonate precursors and the as-annealed product are presented in Figure 1a and 1b, respectively. Both of the as-obtained precursors have similar XRD patterns apart from some differences in the intensity of diffraction peaks. Unlike the previously reported data in the literature, such as $Co(OH)_2$,[16] CoOOH,[17] Co(OH)F,[18,19] $Co(CO_3)_{0.5}(OH)•0.11H_2O$[20, 21] and $CoCO_3$[22-25], the three strong peaks in pattern of the precursors locate at 2θ values of 17.2 °, 23.9 ° and 34.7°, respectively. It is difficult to assign the patterns of the urchin-like precursors to the specific phase, while all the diffraction peaks in pattern of the as-annealed sample can be indexed to a pure cubic phase of Co_3O_4 with Fd3m space group (JCPDS card No. 42-1467) and no impurity was detected (Figure 1b).

Further evidence of the chemical compositions and the element bonding configuration of the precursor and the as-annealed product were collected by X-ray photoelectron spectroscopy (XPS). The binding energies observed in the XPS result were calibrated for samples charging by referencing the C1s peak to 284.8 eV. The survey spectra indicate the presence of Co and O in the two samples (Figure 1c). The Co 2p XPS spectrum of the precursor in Figure 1d shows two sharp peaks with binding energies at 780.9 and 796.9 eV, corresponding to the Co^{2+} coordinated with hydroxyl and carbonate groups and their satellite shake-ups are located at 786.1 and 802.4 eV. The O 1s peak at 531.2 eV can be assigned to the oxygen species in carbonate anion. The small peaks at 289.3 eV in the C 1s spectrum can be attributed to carbonate groups (Figure 1f). The Co 2p peaks at 780.1 and 795.1 eV in the XPS spectra of the as-heated product can be ascribed to Co $2p_{3/2}$ and Co $2p_{1/2}$ of Co_3O_4. The energy difference between Co $2p_{3/2}$ and Co $2p_{1/2}$ splitting is approximately 15 eV, which indicates the existence of both Co^{2+}/Co^{3+} species in the as-prepared cobalt oxide sample. The deconvoluted O 1s spectrum in Figure 1e displays two dominated peaks at 530.0 and 531.6 eV, which can be assigned to the lattice oxygen of spinel Co_3O_4 and the oxygen in hydroxide ions, respectively. The positions of the peaks are in agreement with the results reported elsewhere.[26-30] As shown in Figure S1, energy dispersive X-ray spectroscopy mappings imply the uniform distribution of Co and O elements within the urchins and bundles.

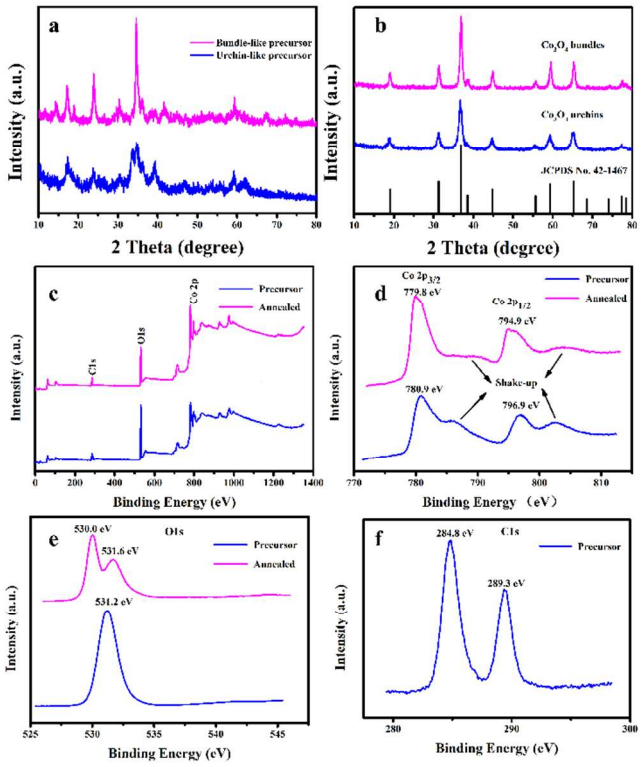

Figure 1. (a) XRD pattern of the urchin-like and bundle-like precursor obtained at 90 °C; (b) XRD pattern of the corresponding mesoporous urchin-like and bundle-like Co_3O_4 after calcination at 400 °C for 4h in air; XPS spectra of bundle-like precursor and

Co_3O_4: (c) survey spectrum; (d) Co 2p; (e) O 1s; (f) C 1s in the precursor.

The thermogravimetric analysis of the two kind of cobalt-hydroxide-carbonate specimens (Figure 2a) illustrates that both of the cobalt-hydroxide-carbonate urchins and bundles show a nearly identical weight loss (about 25%). The first weight loss, which is ascribed to the removal of absorbed water, occurs between 50 and 150 °C. The second weight loss, between 150 and 300 °C, is corresponds to the decomposition of cobalt-hydroxide-carbonate and the formation of cobalt oxide.

Figure 2b shows the FTIR spectra of the cobalt-hydroxide-carbonate precursors and cobalt oxide samples. FTIR spectrum of the two precursors shows similar feature. The bands at 1549 and 1354 cm^{-1} correspond to the stretching vibrations of ν(OCO2) and $\nu(CO_3)$ in the carbonate anion, while the band at 970 cm^{-1} is attributed to the δ(Co-OH) bending vibration.[31,32] As compared with the cobalt-hydroxide-carbonate samples, the IR spectra of the cobalt oxide samples show two distinct bands that originate from the stretching vibrations of the metal–oxygen bonds. The first band at 571 cm^{-1} is associated with the Co^{3+} vibration in an octahedral hole and the second band at 663 cm^{-1} is attributed to the Co^{2+} vibration in a tetrahedral hole in the spinel lattice, which further confirm the formation of the Co_3O_4 spinel. For all FTIR curves of the precursors and the as-calcined samples, the broad absorption band between 3440 and 3500 cm^{-1} and the peak at 1632 cm^{-1} are detected which could be assigned to the O-H stretching and bending vibration of absorbed water and surface hydroxyl groups.[33-37]

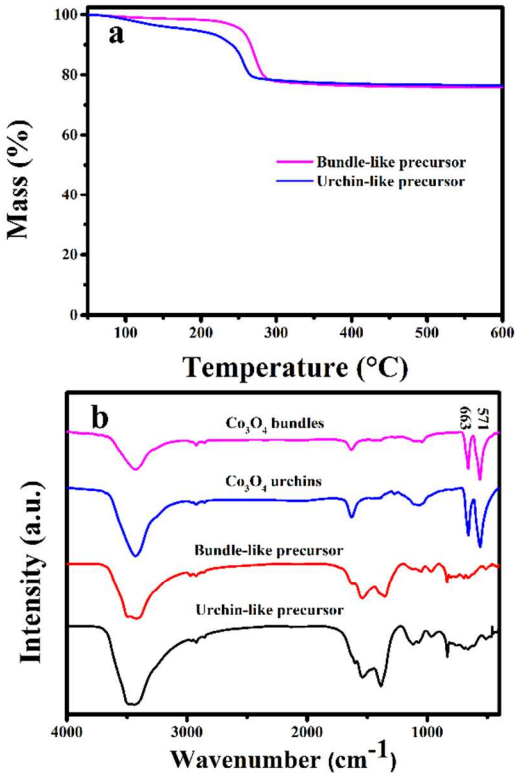

Figure 2 (a) TG profiles of the urchin-like and bundle-like precursor; (b) FTIR spectrum of the precursors and Co_3O_4.

Figure 3 illustrates low- and high-magnification SEM images of the as-obtained precursors, Co_3O_4 urchins and bundles. It can be seen from Figure 3a and 3b that the precursor consists of urchin-like structures assembled by numerous nanowires and their typical size is in the range of 4-5 μm in length. The uniform 3D-bundle structure are observed at first sight in Figure 3c. To reveal the micro-/nanostructures more clearly, high-magnification images are presented in the Figure 3d. The bundles precursors are consist of many interconnected nanobelts, and their typical size is in the range of 5-6 μm in length and 10-30 nm in thickness. Figure 2e-h present that the urchin-like and bundle-like shape does not get changed much and final Co_3O_4 samples after calcination remains similar in morphology. The length and thickness of Co_3O_4 bundles are similar to those of the precursors. The surfaces of those urchins and bundles are both extraordinary rough, which can be ascribed to the release and loss of H_2O and CO_2 during the thermal decomposition.

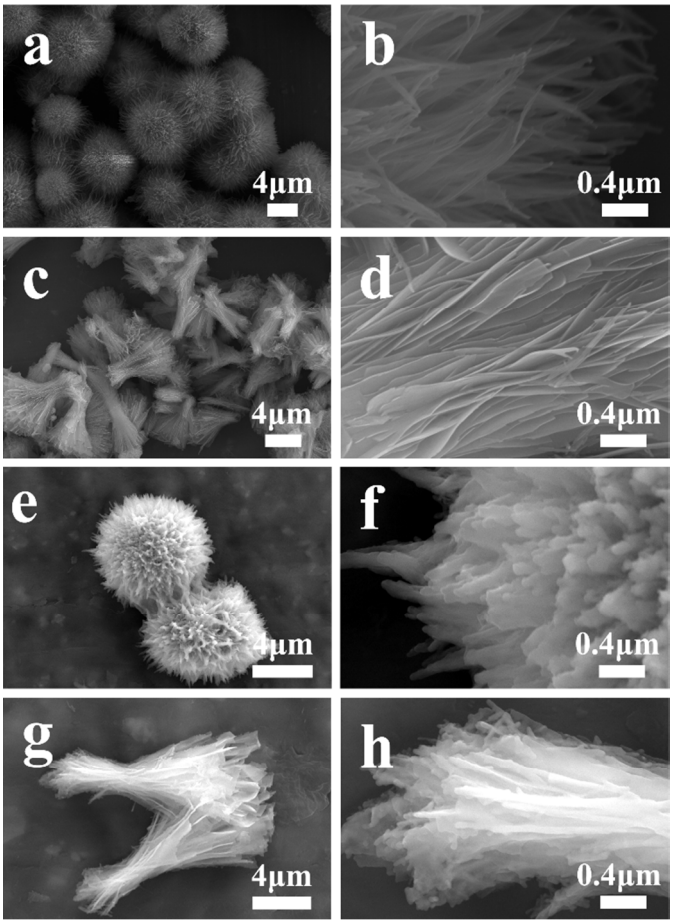

Figure 3 FESEM images of the urchin-like precursor (a, b), bundle-like precursor(c, d), mesoporous urchin-like Co_3O_4 (e, f) and mesoporous bundle-like Co_3O_4 (g, h) at different magnifications.

Apparently, urea acted as the sources of carbonate and hydroxyl ions in this work. Here, a number of CO_3^{2-} and OH^- anions yielded from urea react with Co^{2+} to form cobalt-hydroxide-carbonate

precursor nucleus. According to the reactants, the formation of the cobalt-hydroxide-carbonate precursor can be described as the following formulas: [38, 39]

$$CO(NH_2)_2 + 3H_2O \rightarrow 2NH_4^+ + CO_2 + 2OH^-$$

$$CO_2 + 2OH^- \rightarrow CO_3^{2-} + H_2O$$

$$Co^{2+} + 0.5(2-x)\ CO_3^{2-} + xOH^- + nH_2O \rightarrow Co(OH)_x(CO_3)_{0.5(2-x)} \cdot nH_2O$$

We studied the structure and morphology evolution of this hierarchical sample by performing systematic time-/temperature-dependent experiments.

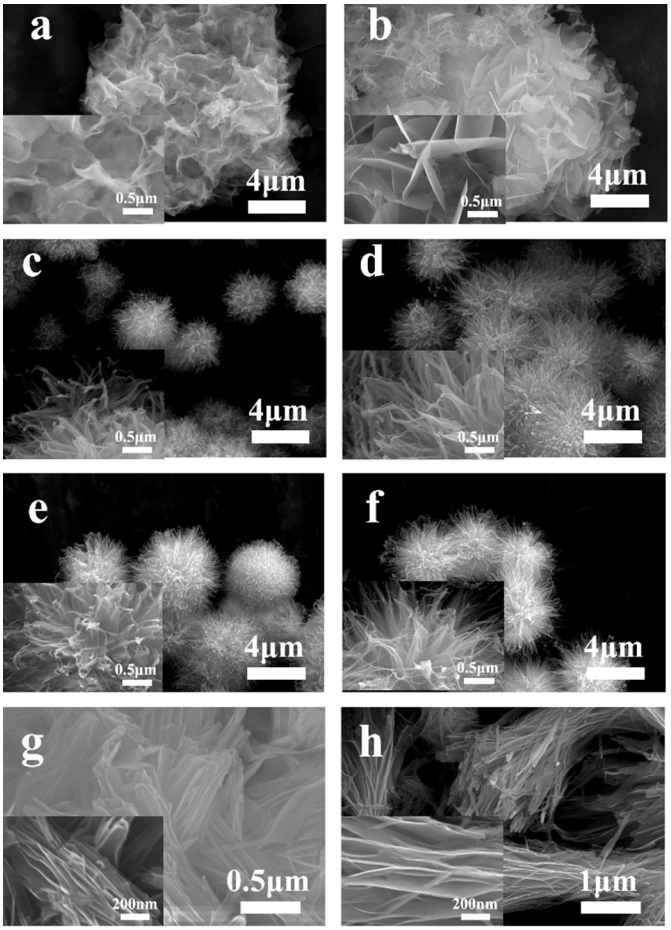

Figure 4 FESEM images of the product synthesized for different times through hydrothermal method: (a) 2.5 h; (b) 3 h; (c) 6 h; (d) 9 h; (e) 12 h; (f) 24 h; (g) 48 h; (h) 72 h. Corresponding insets illustrate higher magnification images.

As it shown in Figure S2, which is the macrograph of the product, the reactants start to deposit at ~2.5 h, and only red solution can be collected before that. It is worth mentioning that the color of the products changes from virescent to purple and finally turns into reddish as reaction time progresses. After reacting for 2.5 h, the as-collected precipitate was comprised of ultrathin nanosheets (Figure 4a and the inset). As the hydrothermal time was prolonged to 3 h, 2D nanosheets further grew (Figure 4b and the inset). Urchin-like structures assembled by numerous slender nanosheets were initially formed at 6 h and finally completed at 36 h along with the further increase in the reaction time (Figure 4f and the inset). When the reaction time was further up to 48 h, the urchin-like precursor were broken and transformed into bundle-like microstructures assembled by the interconnected ultrathin nanosheets (Figure 4g and the inset). And then the morphology of the microstructures became more complete when the reaction time gradually increased to 72-120 h (Figure 4h and the inset). It is note that the thickness of the nanosheets increases along with the extended reaction time. Similar phenomenon can also be detected through temperature-dependent experiments (Supporting Information Figure S3). The morphology of all the products obtained at different temperatures (110-150 °C) transform from nanosheet to urchin-like structures and evolve into bundles finally. However, the regular shape, both urchins and bundles are difficult to achieve at higher hydrothermal reaction temperature. Also the as-obtained urchins with higher size and bundles with the thicker nanosheets at higher temperature could not beneficial for the formation of Co_3O_4 samples with shorter Li^+ ions diffusion paths.

On the basis of the investigations described above, we proposed that the morphology evolution of the precursor was achieved via a two-step growth mechanism, an oriented attachment mechanism and the Ostwald ripening mechanism, [40] as shown in Scheme 1. Firstly, the cobalt-hydroxide-carbonate nuclei combine with each other through spontaneous self-organization to form one-dimensional nanosheets. Then 2D nanosheets are formed through the oriented attachment mechanism and 3D hierarchical urchin-like structures are completed finally through the arrangement. As the crystals grow larger, the increased volume allows the products to coarsen with a decrease in surface energy through the Ostwald ripening mechanism. Therefore, unstable smaller particles dissolve and larger particles grow by adsorbing monomers from the dissolved particles driven by surface energy minimization. The size of the larger particles becomes more and more large until the Ostwald ripening process is under a pseudo-equilibrium state, which is coincide with the previous observations.

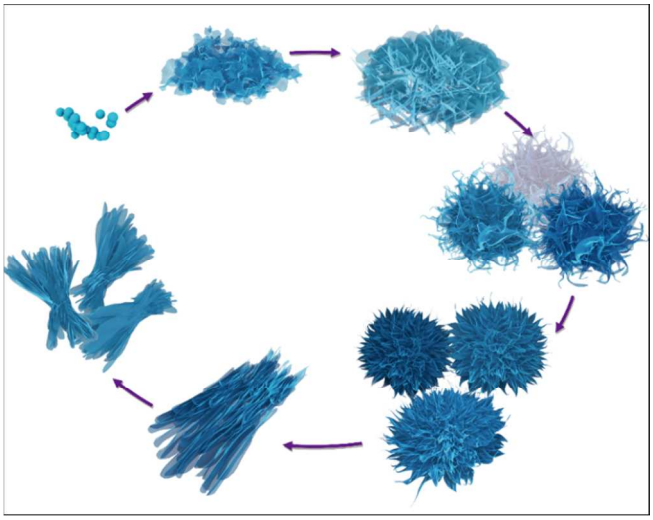

Scheme 1 Schematic representation of the possible formation mechanism of the precursor.

The porous structure characteristics and Brunauer-Emmett-Teller (BET) specific surface area of the u-Co_3O_4 and b-Co_3O_4 were investigated by nitrogen isothermal adsorption isotherms in Figure 5a and 5b, respectively. Both the isotherms display typical IV characteristic and hysteretic loops, which indicating the presence of mespores in the samples. The pore size distribution indicates that the main pore sizes (inset in Figure 5) in the Co_3O_4 urchins and bundles are approximately equal (12.39 and 12.36 nm, respectively). The BET surface area of the u-Co_3O_4 is determined to be 129.70 m^2 g^{-1}, which is higher than that of the bundles (53.19 m^2 g^{-1}). The pore volume which are examined by the nitrogen adsorption-desorption isotherms are 0.565 cm^3 g^{-1} for u-Co_3O_4 and 0.423 cm^3 g^{-1} for b-Co_3O_4, respectively, which means that the void space of u-Co_3O_4 is great than that of b-Co_3O_4.

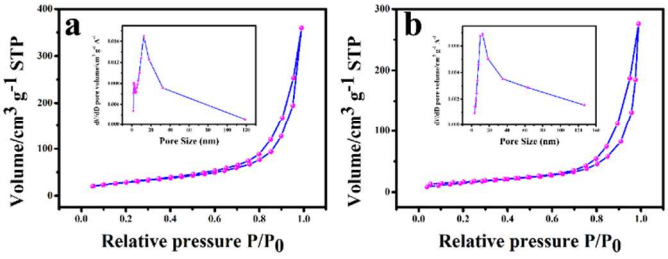

Figure 5 N_2 adsorption-desorption isotherm of the as-obtained urchin-like Co_3O_4 (a) and bundle-like Co_3O_4 (b). Corresponding insets display pore size distribution of the as-obtained Co_3O_4.

The discharge/charge profiles and cycle performance of u-Co_3O_4 and b-Co_3O_4 electrodes by galvanostatic charge-discharge measurements at a current density of 200 mA g^{-1} in a potential window of 0.005-3.0 V were shown in Figure 6. For the u-Co_3O_4 sample, it displays the typical voltage plateau characteristics of transition metal oxides with a short plateau at about 1.0 V, which is related to the partial formation of $Li_xCo_3O_4$ or CoO intermediate phase and always observed for the nano-size particle of high specific surface, [10, 41] and a long plateau at around 0.9 V, which is corresponding to the dominating transformation reaction of the further reduction of Co^{2+} into metallic cobalt and Li_2O. The first discharge and charge capacities are high as 1583 and 983 mA h g^{-1}, giving a Coulombic efficiency of 62.1 %. The initial capacity loss can be attributed to the formation of a solid electrolyte interphase (SEI) layer and the irreversible reaction between Li^+ ions and the electrodes. After five cycles of discharge-charge at 200 mA g^{-1}, the Coulombic efficiency are reached and stabilized to 97% following the charge-discharge cycles. What is noteworthy is that the capacity increases gradually during the subsequent cycles after the initial capacity drop. After 50 cycles, the reversible capacities of the u-Co_3O_4 increase constantly with cycling and the discharge and charge capacities attain 1265 and 1226 mA h g^{-1}. The experimental value exceed the theoretical value, which is common phenomenon for transition metal oxide anode materials, [42] indicating that the polymeric surface layer or gel-like film on the composite electrode may form and the kinetic activation can partially restore for the irreversible Li_2O formed in the first discharge process.[43, 44] In contrast, b-Co_3O_4 electrode exhibits a similar average discharge and charge voltage plateau feature and larger discharge capacity (1624 mA h g^{-1}) with an inferior Coulombic efficiency (60.9% for the first cycle). The capacity also experiences an increases process at subsequent cycles and reach the maximum value (1298 mA h g^{-1}) at the 15th cycle. Then the capacity decays rapidly to 544 mA h g^{-1}. This could be caused by its smaller void space and active surface area, which is also observed in the other report. [39]

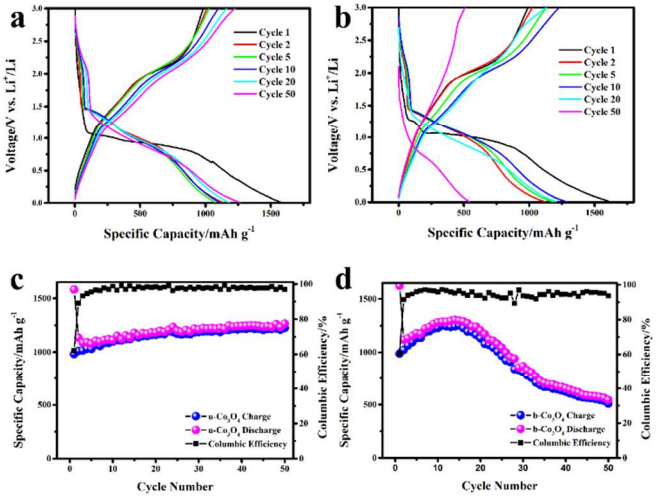

Figure 6 1st, 2nd, 5th, 10th, 20th and 50th cycle of discharge/charge profiles for different samples: (a) mesoporous urchin-like Co_3O_4 electrode and (b) mesoporous bundle-like Co_3O_4 electrode; cyclic performances of the corresponding electrodes at current rate of 200 mA g^{-1}: (c) mesoporous urchin-like Co_3O_4 electrode and (d) mesoporous bundle-like Co_3O_4 electrode.

To fully evaluate the electrochemical properties of the two electrodes as anode materials for LIBs, we examined the rate performance of the electrodes at various rates between 0.1 and 2 A g^{-1} in the range of 0.01-3.0 V *vs* Li/Li^+. The capacities of the u-Co_3O_4 electrode monotonically decrease with increasing current density, as shown in Figure 7a, while these of the b-Co_3O_4 electrode increase initially and then reduce regularly. After each 5 cycles at a specific current rate, the average reversible capacities of the u-Co_3O_4 electrode at 0.1, 0.2, 0.5, 1, and 2 A g^{-1} are about 1114, 1096, 1017, 920, and 781 mA h g^{-1}, respectively, indicating that the rate cycling stability of the Co_3O_4 electrode is excellent. In addition, the b-Co_3O_4 electrode also displays good rate capability with the average discharge capacity of 1148 mA h g^{-1} at 0.1 A g^{-1}, 1219 mA h g^{-1} at 0.2 A g^{-1}, 1173 mA h g^{-1} at 0.5 A g^{-1}, 1040 mA h g^{-1} at 1 A g^{-1}, 660 mA h g^{-1} at 2 A g^{-1}. When the current density returns from 2 to 0.1 A g^{-1}, both the electrodes recovers their original average capacity and even a little higher (1229 mA h g^{-1} for u-Co_3O_4, 1304 mA h g^{-1} for b-Co_3O_4), which is common in the results of other transition metal oxides reported elsewhere. [27, 41, 45-47]

Due to the porous structures present the prominent rate capability, the electrochemical performance at a large current density of 500

mA g^{-1} was further examined, as illustrated in Figure 7b. The first discharge and charge capacities are 1427 and 927 mAh g^{-1} for u-Co_3O_4 electrode with a Coulombic efficiency of 65.0 %, and 1466 and 915 mAh g^{-1} for b-Co_3O_4 electrode, respectively. The discharge capacity of u-Co_3O_4 electrode decrease rapidly to 978 mAh g^{-1} after 3 cycles slightly and then increases slightly to 1027 mAh g^{-1} with a Coulombic efficiency of 97.4 % after 50 cycles. The discharge capacity of b-Co_3O_4 electrode also experiences a process of increase to decrease and deliver 671 mAh g^{-1} after 50 cycles, which is in accordance with that carried out at a current density of 100 mA g^{-1}. It is obvious to conclude that the two electrodes display excellent electrochemical performance, which can be attributed to the dense distribution of pores in their architectures. The high BET surface can offer more active reaction sites, shorten the Li^+ diffusion length and reduce the resistance of electrolyte to obtain superior high-rate performance. The large pore volume provides more space to alleviate the negative influence produced by the volume expansion as the cycling of discharge/charge, thus leading to better structure stability and larger contact area with the electrolyte.

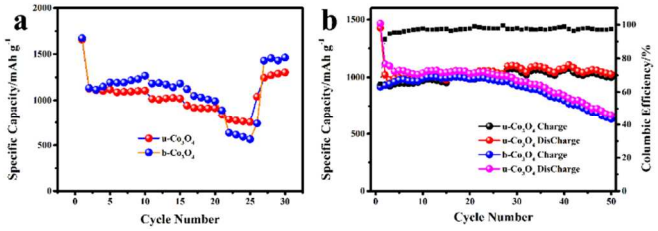

Figure 7 (a) Charge-discharge performance of mesoporous urchin-like and bundle-like Co_3O_4 electrode at various current rates; (b) cyclic performances of the corresponding two electrodes at current rate of 500 mA g^{-1}.

Conclusions

In conclusion, we have demonstrated a general strategy to prepare the mesoporous urchin-like and bundle-like Co_3O_4 architectures. When utilized as the anode material in LIBs, both of them deliver the large initial discharge capacities (1583 mA h g^{-1} for urchin-like Co_3O_4 and 1624 mA h g^{-1} for urchin-like Co_3O_4 at 0.2A g^{-1}, respectively), good cyclic stability and enhanced rate capacity. Considering this enhanced performance and relatively cost-effective synthesis method, we reckon the as-obtained urchin-like and bundle-like might be available as anode electrodes for next generation LIBs.

Acknowledgements

The authors acknowledge the financial support of the Fundamental Research Funds for the Central Universities (Grant No. 2012067), the Program for New Century Excellent Talents in University of Ministry of Education of China (Grant No. NCET-12-0951), the Science and Technology Innovation Funds for graduate students of China University of Geosciences (2012). T. Yang would like to acknowledge financial support from China Scholarship Council.

Notes and references

[a] School of Materials Science and Technology, Beijing Key Laboratory of Materials Utilization of Nonmetallic Minerals and Solid Wastes, National Laboratory of Mineral Materials, China University of Geosciences (Beijing) 100083, P.R. China. *E-mail*: liuyang@cugb.edu.cn; huang118@cugb.edu.cn; *Tel*.: +86-010-82322186, *Fax*: +86-010-82322186.

Electronic Supplementary Information (ESI) available: [SEM images and corresponding EDX element mappings for the hierarchically porous Co_3O_4 urchins and bundles. The macrograph of the as-obtained precursors for different times by hydrothermal method at 90 °C. SEM images of the as-obtained precursor at different temperature with different reaction times. are provided.]. See DOI: 10.1039/b000000x/

1 Reddy, M. V.; Subba Rao, G. V.; Chowdari, B. V. R. Metal oxides and oxysalts as anode materials for Li ion batteries. Chem. Rev. **2013**, 113, 5364-5457.

2 Barré, A.; Deguilhem, B.; Grolleau, S.; Gérard, M.; Suard, F.; Riu, D. A review on lithium-ion battery ageing mechanisms and estimations for automotive applications. J. Power Sources **2013**, 241, 680-689.

3 Bruce, P. G.; Scrosati, B.; Tarascon, J. M. Nanomaterials for rechargeable lithium batteries. Angew. Chem. Int. Ed. **2008**, 47, 2930-2946.

4 Scrosati, B.; Hassoun, J.; Sun, Y. K. Lithium-ion batteries. A look into the future. Energy Environ. Sci., **2011**, 4, 3287-3295.

5 Dunn, B.; Kamath, H.; Tarascon, J. M. Electrical energy storage for the grid: a battery of choices. Science, **2011**, 334, 928-935.

6 Goodenough, J. B.; Kim, Y. Challenges for rechargeable Li batteries. Chem. Mater. **2010**, 22, 587-603.

7 Ji, L.W.; Lin, Z.; Alcoutlabi, M.; Zhang, X. W. Recent developments in nanostructured anode materials for rechargeable lithium-ion batteries. Energy Environ. Sci., **2011**, 4, 2682-2699.

8 Xia, F.F.; Hu, X.L.; Sun Y.M.; Luo, W; Huang, Y.H. Layer-by-layer assembled MoO_2–graphene thin film as a high-capacity and binder-free anode for lithium-ion batteries. Nanoscale, **2012**, 4, 4707-4711.

9 Reddy, M. V.; Rao, G. V. S.; Chowdari, B. V. R. Metal Oxides and Oxysalts as Anode Materials for Li Ion Batteries. Chem. Rev., **2013**, 113, 5364-5457.

10 Poizot, P.; Laruelle, S.; Grugeon, S.; Dupont, L. Tarascon, J-M. Nano-sized transition-metal oxides as negative-electrode materials for lithium-ion batteries. Nature, **2000**, 407, 496-499.

11 Yang, T.; Liu, Y.G.; Huang, Z.H.; Yang, Q.; Chen, Y.B.; Hu, M.L.; Guan, M.; Fang, M.H. Porous Peony-like α-Fe_2O_3 Hierarchical Micro/nanostructures: Synthesis, Characterization and its Lithium Storage Properties. RSC Adv., **2014**, 4, 41578-41583.

12 Luo, W; Hu, X.L.; Sun Y.M.; Huang, Y.H. Electrospun porous $ZnCo_2O_4$ nanotubes as a high-performance anode material for lithium-ion batteries. J. Mater. Chem., **2012**, 22, 8916-8921.

13 Sun Y.M.; Hu, X.L.; Luo, W; Huang, Y.H. Self-assembled mesoporous CoO nanodisks as a long-life anode material for lithium-ion batteries. J.

Mater. Chem., **2012**, 22, 13826-13831.

14 Qiu, D. F.; Bu, G.; Zhao, B.; Lin, Z.X.; Pu, L.; Pan, L.J.; Shi, Y. In situ growth of mesoporous Co_3O_4 nanoparticles on graphene as a high-performance anode material for lithium-ion batteries. Mater. Lett., 2014, 119, 12-15.

15 Huang, H.; Zhu, W.J.; Tao, X.Y.; Xia, Y.; Yu, Z.Y.; Fang, J.W.; Gan, Y.P.; Zhang, W.K. Nanocrystal-constructed mesoporous single-crystalline Co_3O_4 nanobelts with superior rate capability for advanced lithium-ion batteries. ACS Appl. Mater. Interfaces, **2012**, 4, 5974–5980.

16 Yang, W.L.; Gao, Z.; Ma, J.; Zhang, X.M.; Wang, J. Controlled synthesis of Co_3O_4 and Co_3O_4@MnO_2 nanoarchitectures and their electrochemical capacitor application. J. Alloy Compd. **2014**, 611, 171-178.

17 Zhao, J.; Zou, Y.C.; Zou, X.X.; Bai, T.Y.; Liu, Y.P.; Gao, R.Q.; Wang, D.J.; Li, G.-D.. Self-template construction of hollow CoO microspheres from porous ultrathin nanosheets and efficient noble metal-free water oxidation catalysts. Nanoscale, **2014**, 6, 7255-7262.

18 Zhu, Y. G.; Wang, Y.; Shi, Y.M.; Huang, Z. X.; Fu, L.; Yang, H. Y. Phase transformation induced capacitance activation for 3D graphene-CoO nanorod pseudocapacitor. Adv. Energy Mater. **2014**, 1301788.

19 Wu, F.F.; Ma, X.J.; Feng, J.K.; Qian, Y.T.; Xiong, S.L. 3D Co_3O_4 and CoO@C wall arrays: morphology control, formation mechanism, and lithium-storage properties. J. Mater. Chem. A, **2014**, 2, 11597-11605.

20 Wang, B.; Zhu, T.; Wu, H. B.; Xu, R.; Chen, J. S.; Lou, X. W. (David). Porous Co_3O_4 nanowires derived from long $Co(CO_3)0.5(OH)\cdot 0.11H_2O$ nanowires with improved supercapacitive properties. Nanoscale, **2012**, 4, 2145-2149.

21 Wang, Y.; Xia, H.; Lu, L.; Lin, J.Y. Excellent performance in lithium-ion battery anodes rational synthesis of $Co(CO_3)0.5(OH)\cdot 0.11H_2O$ nanobelt array and its conversion into mesoporous and single-crystal Co_3O_4. ACS Nano, **2010**, 4, 1425-1432.

22 Huang, G.Y.; Xu, S.M.; Lu, S.S.; Li, L.Y.; Sun, H.Y. Micro-/Nanostructured Co_3O_4 anode with enhanced rate capability for Lithium-Ion batteries. ACS Appl. Mater. Interfaces, **2014**, 6, 7236-7243.

23 Li, C.C.; Yin, X.M.; Wang, T.H.; Zeng, H.C. Morphogenesis of highly uniform $CoCO_3$ submicrometer crystals and their conversion to mesoporous Co_3O_4 for gas-sensing applications. Chem. Mater. **2009**, 21, 4984-4992.

24 Du, H.M.; Jiao, L.F.; Wang, Q.H.; Huan, Q.N.; Guo, L.J.; Si, Y.C.; Wang, Y.J.; Yuan, H.T. Morphology control of $CoCO_3$ crystals and their conversion to mesoporous Co_3O_4 for alkaline rechargeable batteries application. CrystEngComm **2013**, 15, 6101-6109.

25 Bian, S.-W.; Zhu, L. Template-free synthesis of mesoporous Co_3O_4 with controlled morphologies for lithium ion batteries. RSC Adv. **2013**, 3, 4212-4215.

26 Li, C.; Yin, X.; Chen, L.; Li, Q.; Wang, T. Synthesis of cobalt ion-based coordination polymer nanowires and their conversion into porous Co_3O_4 nanowires with good lithium storage properties. Chem. Eur. J. **2010**, 16, 5215-5221.

27 Zhan, L.; Wang, S.Q.; Ding, L.-X.; Li, Z.; Wang, H.H. Grass-like Co_3O_4 nanowire arrays anode with high rate capability and excellent cycling stability for lithium-ion batteries. Electrochim. Acta **2014**,135, 35-41.

28 Zheng, F.C.; Zhu, D.Q.; Chen, Q.W. Facile fabrication of porous $Ni_xCo_{3-x}O_4$ nanosheets with enhanced electrochemical performance as anode materials for li-ion batteries. ACS Appl. Mater. Interfaces **2014**, 6, 9256-9264.

29 Zhang, Y. Q.; Li, L.; Shi, S. J.; Xiong, Q. Q.; Zhao, X. Y.; Wang, X. L.; Gu, C. D.; Tu, J. P. Synthesis of porous Co_3O_4 nanoflake array and its temperature behavior as pseudo-capacitor electrode. J. Power Sources **2014**, 256, 200-205.

30 Qiao, R.; Zhang, X.L.; Qiu, R.; Kim, J.C.; Kang, Y.S. Preparation of Magnetic Hybrid Copolymer–Cobalt Hierarchical Hollow Spheres by Localized Ostwald Ripening. Chem. Mater. **2007**, 19, 6485–6491.

31 Jia, G.; Yang, M.; Song, Y.; You, H.; Zhan, H. General and Facile Method To Prepare Uniform Y_2O_3: Eu Hollow Microspheres. Cryst. Growth Des. **2009**, 9, 301-307.

32 Alken, B.; Hsu, W.; Matijevic, E. Preparation and Properties of Monodispersed Colloidal Particles of Lanthanide Compounds: III, Yttrium(III) and Mixed Yttrium(III)/Cerium(III) Systems. J. Am. Ceram. Soc. **1988**, 71, 845-853.

33 Ozkaya, T.; Baykal, A.; Toprak, M.S.; Koseoglu, Y.; Durmus, Z. Reflux synthesis of Co_3O_4 nanoparticles and its magnetic characterization. J. Magn. Magn. Mater. **2009**, 321, 2145-2149.

34 Christokova, S.G.; Stayonava, M.; Georgieva, M.; Mehandjiev, D. Preparation and characterization of a higher cobalt oxide. Mater. Chem. Phys. **1999**, 60, 39-43.

35 Liu, X.M.; Zhang, X.G.; Fu, S.Y. Preparation of urchinlike NiO nanostructures and their electrochemical capacitive behaviors. Mater. Res. Bull. **2006**, 41, 620-627.

36 Yan, Q.Y.; Li, X.Y.; Zhao, Q.D.; Chen, G.H. Shape-controlled fabrication of the porous Co_3O_4 nanoflower clusters for efficient catalytic oxidation of gaseous toluene. Journal of Hazardous Materials. **2012**, 209-210, 385-391.

37 Jiang, J.; Liu, J.P.; Ding, R.M.; Ji, X.X.; Hu, Y.Y.; Li, X.; Hu, A.Z.; Wu, F.; Zhu, Z.H.; Huang, X.T. Direct synthesis of CoO Porous Nanowire Arrays on Ti substrate and their application as lithium-ion battery electrodes. J. Phys. Chem. C **2010**, 114, 929-932.

38 Xu, R.; Zeng, H.C. Dimensional control of Cobalt-hydroxide-carbonate nanorods and their thermal conversion to one-dimensional arrays of Co_3O_4 nanoparticles. J. Phys. Chem. B **2003**, 107, 12643-12649.

39 Sun, P.; Zhao, W.; Cao, Y.; Guan, Y.; Sun, Y.F.; Lu, G.Y. Porous SnO_2 hierarchical nanosheets: hydrothermal preparation, growth mechanism, and gas sensing properties. CrystEngComm **2011**, 13, 3718-3724.

40 Larcher, D.; Sudant, G.; Leriche, J.B.; Chabre, Y.; Tarascon, J.M. The electrochemical reduction of Co_3O_4 in a lithium cell. J. Electrochem.

Soc. **2002**, 149, A234-A241.

41 Wen, J.-W.; Zhang, D.-W.; Zang, Y.; Sun, X.; Cheng, B. C.-X.; Yu, Y.; Chen, C.-H. Li and Na storage behavior of bowl-like hollow Co_3O_4 microspheres as an anode material for lithium-ion and sodium-ion batteries. Electrochim. Acta **2014**, 132,193-199.

42 Laruelle, S.; Grugeon, S.; Poizot, P.; Dollé, M.; Dupont, L.; Tarascon, J.M. On the origin of the extra electrochemical capacity displayed by MO/Li cells at low potential. J. Electrochem. Soc. **2002**, 149, A627-A634.

43 Do, J.S.; Weng, C.H. Preparation and characterization of CoO used as anodic material of lithium battery. J. Power Sources **2005**, 146, 482-486.

44 Chen, J. S.; Zhu, T.; Hu, Q. H.; Gao, J.; Su, F.; Qiao, S. Z.; Lou, X. W. Shape-controlled synthesis of cobalt-based nanocubes, nanodiscs, and nanoflowers and their comparative lithium-storage properties. ACS Appl. Mater. Interfaces **2010**, 2, 3628-3635.

45 Sun, H.T.; Sun, X.; Hu, T.; Yu, M.P.; Lu, F.Y.; Lian, J. Graphene-Wrapped Mesoporous Cobalt Oxide Hollow Spheres Anode for High-Rate and Long-Life Lithium Ion Batteries. J. Phys. Chem. C **2014**, 118, 2263-2272.

46 Shen, L.S.; C.X. Wang. Hierarchical Co_3O_4 Nanoparticles Embedded in a Carbon Matrix for Lithium-Ion Battery Anode Materials. Electrochim. Acta **2014**, 133, 16-22.

47 Pan, A.Q.; Wang, Y.P.; Xu, W.; Nie, Z.W.; Liang, S.Q.; Nie, Z.M.; Wang, C.M.; Cao, G.Z.; Zhang, J.G. High-performance anode based on porous Co_3O_4 nanodiscs. J. Power Sources **2014**, 255, 125-129.

